PHYSICAL REVIEW B **82**, 054401 (2010)

Contrasted role of disorder for magnetic properties in an original mixed-valency iron phosphate

Laure Adam, Alain Pautrat, Olivier Perez, and Philippe Boullay
Laboratoire CRISMAT, UMR 6508 du CNRS, ENSICAEN et Université de Caen, 6 Bd Maréchal Juin, F-14050 Caen 4, France

(Received 21 May 2010; published 2 August 2010)

We have measured the magnetic properties of a mixed-valency iron phosphate. It presents an original structure with crossed chains containing Fe^{II} and orthogonal to the longest direction of the crystallites. Microstructural investigations using electron microscopy show the presence of random nanotwinning. The ac susceptibility measurements demonstrate similarities with the kinetics of a disordered magnetic, spin-glasslike state but are shown to be essentially due to this peculiar disorder. Scaling properties are characteristics of three-dimensional second-order transition implying that this disorder at a small scale does not influence significantly long-range magnetic ordering. At low temperature, a decrease in the spontaneous magnetization and an irreversible metamagnetic transition is observed, and is attributed to a canting of the spins in the iron chain.

DOI: 10.1103/PhysRevB.82.054401 PACS number(s): 75.50.−y, 75.30.Kz, 68.37.Ef, 61.50.−f

I. INTRODUCTION

Transition-metal phosphates constitute a great family of compounds widely investigated because of their various potential applications, such as cathodes for Li batteries,[1] heterogeneous catalysts,[2] or molecular sieves.[3] Magnetic properties are less deeply studied although structural features of many reported phases (e.g., metal polymers, infinite chains of metal polyhedra) suggest interesting, albeit complex, magnetic interactions. Indeed, the structural features mixes low dimensionality, disorder and, more rarely, different valencies which may lead to different spin sublattices. Up to now, vanadium phosphates still seem to be the most investigated.[4–6] Others transition-metal phosphates are obviously studied such as copper phosphates[7,8] or manganese phosphates, for instance.[9] Focusing on the iron phosphate group, an antiferromagnetic behavior is reported for $Fe_2P_2O_7$ (superexchange mechanism between Fe^{II}),[10] Fe_3PO_7 (direct exchange or superexchange mechanisms between Fe^{III}),[11] and $Fe_4(P_2O_7)_3$ (superexchange mechanism between Fe^{III}).[12] $SrFe_2(PO_4)_2$, which framework exhibits iron tetramers in the high spin Fe^{II} state, present more complex magnetic properties, including metamagnetic regimes and competition between structural and magnetic phase transitions.[13,14] A study by powder neutron diffraction of β-$Fe_2(PO_4)O$, which three-dimensional (3D) framework is built of iron polyhedra infinite chains, revealed a ferromagnetic order within the chains and an antiferromagnetic order between the chains which leads to an antiferromagnetic bulk transition.[15] One interesting aspect of transition-metal phosphates for magnetism is that phosphate groups can isolate magnetic ions, leading to low-dimensional spin systems. Another interesting aspect, maybe less deeply studied, is that original structures with a nontrivial disorder can be stabilized. As we will show here, such a peculiar disorder can have important consequences with, for example, an averaging of low-dimensional magnetic characteristics at the sample scale. Then, coupling a careful analysis of structural data with detailed magnetic measurements will help to shed some light on the role of specific geometries for magnetic properties of disordered medium.

We report herein on the study of magnetic properties in the original mixed-valency iron phosphate β-$(NH_4)Fe_2(PO_4)_2$ using macroscopic magnetic measurements. The study by x-ray diffraction of its structure has already been reported[16] so that only a brief reminder of the structural main features will be given. An additional study using electron microscopy allows a better understanding of the disorder phenomenon at a local scale and its influence on the magnetic properties, which reveal interesting features such as slow dynamics due to the peculiar disorder of the structure and canting of the spins at low temperature.

II. SAMPLE PREPARATION AND STRUCTURAL ANALYSIS

A single-phase sample of β-$(NH_4)Fe_2(PO_4)_2$ was prepared under hydrothermal conditions. A mixture of Fe_2O_3, $FeCl_2$, and $(NH_4)_2HPO_4$, in the respective molar ratio 0.25:0.5:1, was placed in a 21 mL Teflon-lined stainless-steel autoclave with 2 mL of deionized water. It was heated at 493 K over 25 h and then cooled to room temperature for 17 h. The resulting product, made up of black needlelike crystals of β-$(NH_4)Fe_2(PO_4)_2$ (Fig. 1), was filtered and washed with deionized water. The phosphate β-$(NH_4)Fe_2(PO_4)_2$ was then characterized using single-crystal x-ray diffraction, and crystallizes in the orthorhombic space group F_{ddd} with the cell parameters $a=17.1491(2)$ Å, $b=7.4419(2)$ Å, and $c=10.0522(3)$ Å. Detailed characterization using superspace formalism was previously proposed.[16] In particular, the presence of diffuse scattering characteristic of correlated disorder was reported. The three-dimensional framework of β-$(NH_4)Fe_2(PO_4)_2$ is built of distorted $Fe^{II}O_6$ and $Fe^{III}O_6$ octahedra and PO_4 tetrahedra. Theses polyhedra share edges and apices to form hexagonal tunnels, running along [011] and $[0\bar{1}1]$ directions, in which ammonium cations are located (Fig. 2). Projections of the structure along [011] and $[0\bar{1}1]$ directions show that $[FeP_2O_8]_\infty$ ribbons are running along [011] and $[0\bar{1}1]$ directions (Fig. 2), i.e., perpendicularly to the needlelike crystal axis $\vec{a}$; the angle between two ribbons being 73° (Fig. 3). Each $[FeP_2O_8]_\infty$ ribbon is made of edge-sharing $Fe^{II}O_6$ and PO_4 polyhedra; the role of the $[FeO_4]_\infty$ chains (Fig. 2) will be discussed in the analysis of the magnetic properties. $[FeP_2O_8]_\infty$ ribbons are connected to

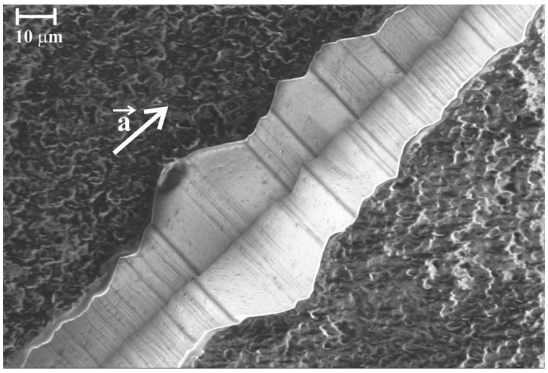

FIG. 1. Scanning electron microscope (SEM) picture of a needlelike crystallite of β-$(NH_4)Fe_2(PO_4)_2$, with the direction of the a axis.

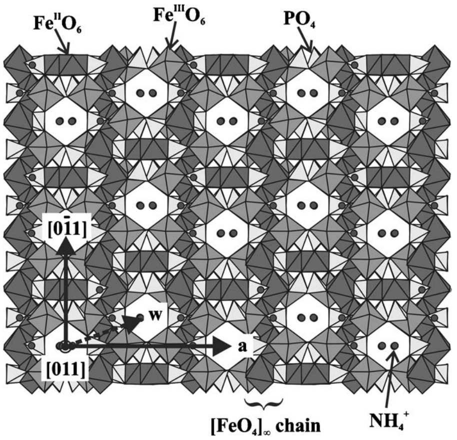

FIG. 2. Projection of the β-$(NH_4)Fe_2(PO_4)_2$ structure along [011].

each other thanks to $Fe^{II}O_6$ octahedra and PO_4 tetrahedra. As a consequence, one $Fe^{II}O_6$ octahedron share one edge with one PO_4 tetrahedron, four apices with four other PO_4 tetrahedra and two apices with two $Fe^{III}O_6$ octahedra. The $Fe^{III}O_6$ octahedra running along [011] and $[0\bar{1}1]$ directions, i.e., the ordered part of this complex structure, form hexagonal tunnels containing NH^{4+} cations alternate with $[FeO_4]_8$ chains according to the sequence NH^{4+}-$[FeO_4]_8$-NH^{4+}-$[FeO_4]_8$ (Fig. 2). Nevertheless, a random distribution of hexagonal tunnels and $[FeO_4]_8$ chains can be observed along the $\vec{w}$ direction, i.e., $[2\bar{1}\bar{1}]$. Such an impossibility to define a fixed sequence along this direction indicates that β-$(NH_4)Fe_2(PO_4)_2$ exhibits a complex disorder phenomenon along $\vec{a}$.

III. MICROSTRUCTURAL ANALYSIS USING TRANSMISSION ELECTRON MICROSCOPY

In order to obtain further information on the nature of this disorder at a local scale, we decided to investigate β-$(NH_4)Fe_2(PO_4)_2$ by transmission electron microscopy (TEM) using a JEOL2010F microscope. Part of the product of the hydrothermal synthesis was crushed in an agate mortar to obtain small fragments that were put in a suspension in alcohol. A drop of the suspension was then deposited and dried on a copper grid previously coated with a thin film of amorphous carbon. Selected area electron diffraction (SAED) performed on several crystallites confirms that β-$(NH_4)Fe_2(PO_4)_2$ presents a disordered structure evidenced on the diffraction patterns by the systematic presence of diffuse scattering along the $[100]^*$ direction.

As mentioned above, the [011] projection (Fig. 2) appears the one to choose to obtain information on how the hexagonal tunnels are filled: either with NH_4^+ groups or with $[FeP_2O_4]_\infty$ ribbons. In Fig. 4(a), a typical [011] SAED zone axis patterns (ZAPs) show spots that can be indexed considering the F_{ddd} orthorhombic unit cell previously reported[16] [Fig. 4(b)]. Figure 4(a) also reveals the existence of strong diffuse streaks (marked with white arrows) parallel to $[100]^*$ and located in between the spots rows. In addition, depending on the crystallite under observation, more or less pronounced intensity reinforcement in the form of nodes elongated along $[100]^*$ can be observed at positions that could be indexed considering a slightly distorted [112] ZAP of the $H < H^*$ monoclinic unit cell[17] [Fig. 4(c)]. Keeping in mind that our goal was to reveal how the $[FeP_2O_4]_\infty$ ribbons are locally arranged in the structure and also considering that this compound was beam sensitive, we choose to gain information at a local scale working at a medium resolution in the TEM imaging mode. Using an objective aperture to select diffraction scattered at an angle corresponding to a ~5 Å resolution limit [see light gray circle in Fig. 4(a)], we form an image with only few beams but with the most intense part of the diffuse scattering. The structure of the ordered α-$(NH_4)Fe_2(PO_4)_2$ was used to simulate the TEM images (JEMS software) and verify that in such an operating condition the images actually allow exclusively to reveal the arrangement of the hexagonal tunnels (separated at least by 6 Å). Additionally there is a large focal range where the hexagonal tunnels filled with NH_4^+ groups appear as bright intense dots for thicknesses above 10 nm. The experimental image in Fig. 5 shows a crystallite heavily twinned at the nanoscale with a twin plane perpendicular to the [100] direction. Figure 5(a) is a Fourier filtered image constructed by selecting only the six spots present in the Fourier diffractogram of the experimental image and operating an inverse Fourier transformation. Such an image actually represents the arrangement of the hexagonal tunnels regardless their

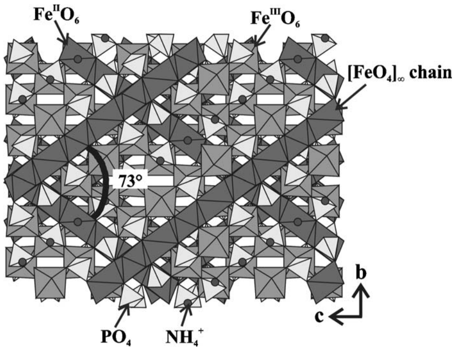

FIG. 3. Projection of the β-$(NH_4)Fe_2(PO_4)_2$ structure along the a axis [i.e., perpendicularly to the (bc) plane].

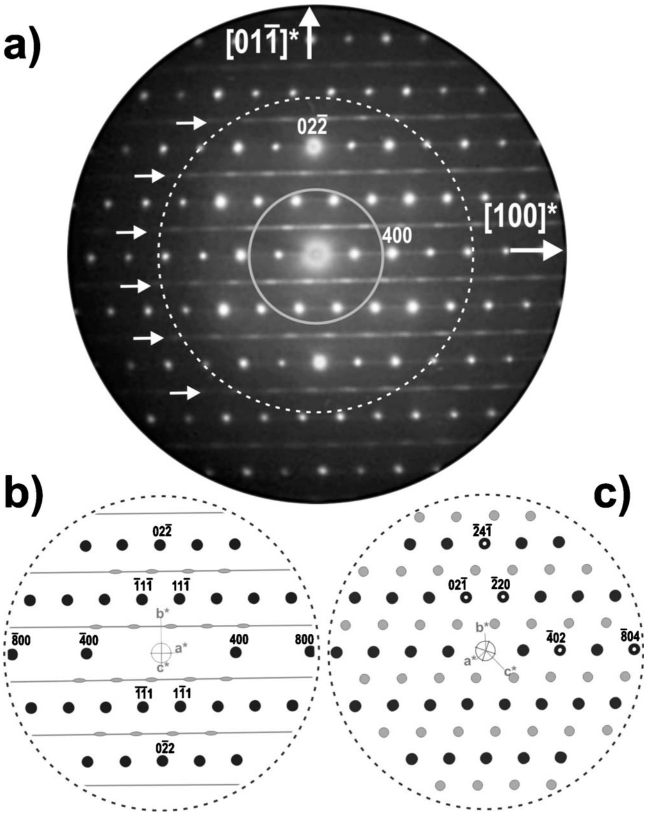

FIG. 4. (a) [011] SAED zone axis patterns observed on a β-$(NH_4)Fe_2(PO_4)_2$ crystallite. It can be described as the regular alternation along $[01\bar{1}]^*$ of two type of rows parallel to $[100]^*$ one being diffuse streaks at $d^*=\mathrm{o}\cdot\frac{1}{2}\cdot d^*_{01\bar{1}}$ (o for odd integer) and the other made of spots at $d^*=n\cdot d^*_{01\bar{1}}$. (b) Schematic representation of the dashed circular area in (a) and where the spots (in dark) related to the average structure are indexed considering the F_{ddd} orthorhombic cell. In gray is represented the diffuse streaks where intensity reinforcement can be observed. (c) The diffuse nodes can actually be indexed considering a [112] ZAP of the α-$(NH_4)Fe_2(PO_4)_2$ ordered monoclinic form (Ref. 17).

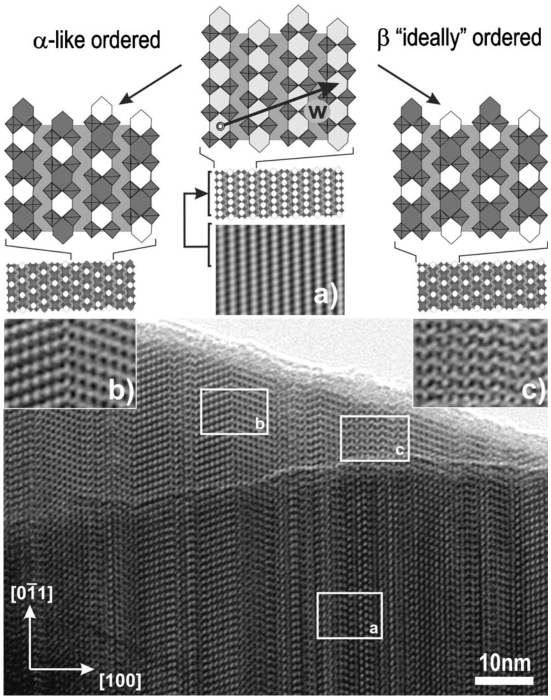

FIG. 5. ∼5 Å resolution TEM image obtained from a β-$(NH_4)Fe_2(PO_4)_2$ crystallite. (a) Fourier filtered image generated by selecting only the spots present in the diffractogram observed in the Fourier transform of the *a* area. Such an image allow to locate the hexagonal tunnels present in the structure regardless how they are filled as illustrated in the schematic structure drawing above the image. Depending on the filling sequence along $\mathbf{w}\sim[2\bar{1}1]$ between NH_4^+ groups (white hexagon) and $[FeO_4]_\infty$ chains (dark gray hexagon), it is possible to generate either a α- or β-type ordering. (b) Enlargement (×2) of the experimental image (*b* area) showing that this part of the crystal can be seen as a α-$(NH_4)Fe_2(PO_4)_2$ twin structure at a nanoscale. (c) Enlargement (×2) of the experimental image (*c* area) showing that locally this part of the crystal can be seen as an ideally β-$(NH_4)Fe_2(PO_4)_2$ ordered structure.

occupancy [see schematic representation above Fig. 5(a)]. It do not exhibit any twinning and the periodicity along $[0\bar{1}1]$ is half the one observed in the experimental image. It shows that the arrangement of the hexagonal tunnels is identical all over the experimental image, only the way they are filled up differs. Importantly, this last information is carried on by the diffuse streaks and can be related, in the image mode, to the observed twinning. The enlarged parts of the experimental image in Figs. 5(b) and 5(c) show two different types of nanostructure. The first one Fig. 5(b) corresponds to a twin structure where the hexagonal tunnels are filled following the sequence NH_4^+-$[FeP_2O_4]_\infty$-NH_4^+-$[FeP_2O_4]_\infty$ along the direction $\mathbf{w}\sim[2\bar{1}1]$. This sequence is related to the stacking found in the ordered α-$(NH_4)Fe_2(PO_4)_2$. The second one Fig. 5(c) corresponds locally to a structure where the hexagonal tunnels are filled following the sequence NH_4^+-NH_4^+-$[FeP_2O_4]_\infty$-$[FeP_2O_4]_\infty$ along the direction $\mathbf{w}$, which is related to the ideally ordered $T=23$ reported in Ref. 16. The disordered structure of β-$(NH_4)Fe_2(PO_4)_2$ explored at this local scale is thus fully consistent with the conclusion previously drawn from the single-crystal x-ray diffraction. Locally each platelet presents a filling sequence in the hexagonal tunnels that can be related either to the α-type ordering with different twinned domains or the "ideally" β-type ordering, which can be considered as polytypes of $NH_4Fe_2(PO_4)_2$. The arrangement of NH_4^+ groups and $[FeP_2O_4]_\infty$ ribbons is ordered along the $[0\bar{1}1]$ direction with a sequence NH_4^+-$[FeP_2O_4]_\infty$ [see schematic drawing in Figs. 5(b) and 5(c)]. The diffuse scattering originates from the absence of $NH_4^+/[FeP_2O_4]_\infty$ long-range ordering along [100] with the intergrowth of polytype structures and formation of twinning at a nanoscale in the form of infinite platelets developed along $[0\bar{1}1]$ and of limited and random extension along [100].

IV. MAGNETIC PROPERTIES

A. General characterization with dc magnetization

A 1.57 mg amount of randomly oriented crystals was used for studying of magnetic properties. Measurements were

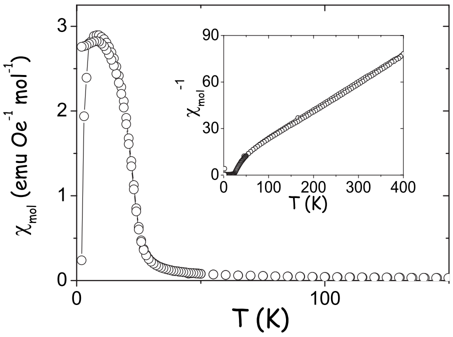

FIG. 6. Molar magnetic susceptibility as a function of the temperature measured during field-cooling and zero-field-cooling procedures with an applied field of 0.1 T. In the inset is shown the inverse molar susceptibility to evidence the Curie-Weiss regime at high temperature.

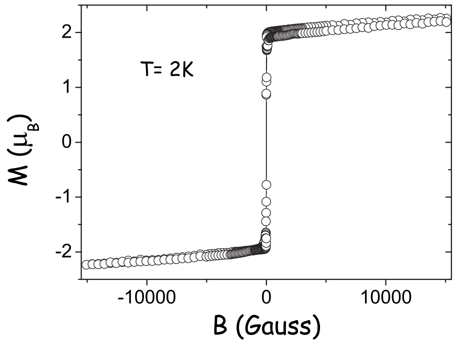

FIG. 7. Magnetic cycle after saturation of the magnetization measured for a temperature $T=2$ K. The magnetization is per formula unit.

made in a magnetic properties measurement system (MPMS) and using the ac susceptibility/dc magnetization measurement system (ACMS) of a physical properties measurement system (PPMS) from Quantum Design. Note that to check that our samples behave as a powder of randomly distributed crystallites, some measurements on a compacted pure powder of the same phosphate were also conducted, and they produced similar results. First magnetic characterizations were made using measurements of the dc magnetization. In Fig. 6 is shown the field-cooled-zero-field-cooled (FC-ZFC) thermal magnetization with an applied field of $B=0.1$ T. Different features can be observed. At $T\approx 24$ K, a large increase in the FC magnetization is observed, suggesting a ferromagnetic or ferrimagnetic ordering. At lowest temperature, the FC and ZFC curves separate, and show thermal hysteresis. A small decrease in the FC magnetization can be observed, below a temperature $T\approx 8$ K. A Curie-Weiss plot of the susceptibility $\chi^{-1}=C/(T-\theta_c)$ gives the following parameters: $\theta_c=-33.6\pm 0.4$ K showing antiferromagnetic correlations and $\mu_{eff}=7.12\pm 0.06$ μ_B/f.u. This latter value is close to one Fe^{II} and one Fe^{III} in a high spin state ($\mu_{eff}=7.68\mu_B$). This proportion of Fe^{II}/Fe^{III} is in agreement with both the structural resolution and the Mossbauer measurements at room temperature (not shown here).

The magnetic cycle at $T=2$ K has a clear ferromagnetic-like signature (Fig. 7) after the first magnetization curve, with a very low coercivity of $H_c\sim 10$ G classifying our material as a soft magnet. At the maximum of the magnetic field available in our superconducting quantum interference device MPMS, the magnetization is not fully saturated [$M(H=5\ \text{T})\sim 2.75$ μ_B/f.u.]. Complementary measurements in a 14 T PPMS using the ACMS option shows that $M_{sat}\sim 3$ μ_B/f.u. for $H\geq 9$ T. This is much lower than the value of 9 μ_B/f.u. expected for fully polarized Fe^{II} and Fe^{III} in the high spin state. From this, a ferrimagnetic ordering can be suspected. Note that the $\chi^{-1}(T)$ curve has a peculiar rounded shape above the transition temperature (inset of Fig. 6) which is also typical of a ferrimagnetic ground state.

B. Frequency-dependent susceptibility

The frequency-dependent susceptibility is a classical tool to characterize disordered magnetic states. For instance, the measure of the shift ΔT of the susceptibility maximum for different frequencies f is an usual procedure to evidence glassylike features. The parameter $\alpha=\Delta T/T_0\log(2\pi f)$ is often used as a phenomenological classification of disordered magnetic states.[18] We have measured the ac suceptibility with applied frequencies ranging from $f=1$ Hz to 1 KHz. We observe a shift of the susceptibility maximum (Fig. 8), and calculate $\alpha\approx 3\times 10^{-3}$, which defines apparently our transition as a spin-glass one.[18,19] It is however clear from the preceding paragraph that our sample has a ferromagnetic characteristic with a permanent moment, and by definition cannot be a spin glass. A well-known property of spin glasses, the aging effect,[20] is not also observed (the relaxation of the magnetization is found to be independent of the time spent at a constant temperature before cutting the field). To understand the reason of the slow dynamics observed with the ac susceptibility, we have first studied the variation in the transition temperature T_m when the applied magnetic field is increased (Fig. 9). This variation is nonmonotonic. At low field $H<H^*\approx 300$ G, T_m decreases when H increases.[21] For $H>H^*$, the opposite field dependency is observed: T_m is an increasing function with H. This latter evolution, and the observed broadening of the transition region, is expected for the critical region of a second-order transition, and is then consistent with a conventional ferromagnetic transition. The question is clearly what is the cause of the low-field behavior ($H<H^*\approx 300$ G) which mimics the slow dynamic of a spin glass around the transition temperature. To answer to this

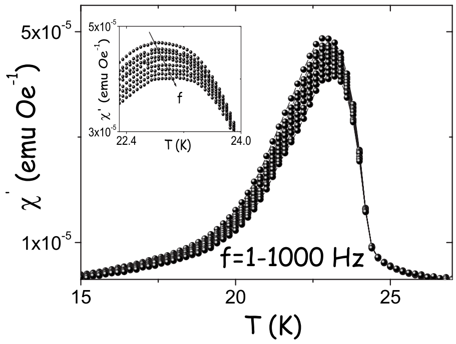

FIG. 8. ac susceptibility for $H=0$ and for different frequencies $f=1$, 5, 10, 25, 50, 120, 250, 500, and 1000 Hz. In the inset are shown similar measurements, taken with small temperature steps.

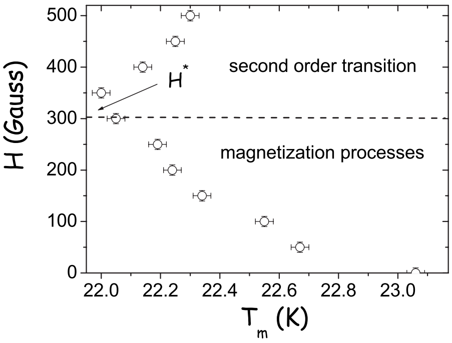

FIG. 9. Applied magnetic field as a function of the temperature of the maximum of susceptibility ($f=7$ Hz). Note the inversion of the dependence at $H=H^{*}\sim 300$ G.

question, we have measured the dc magnetization as a function of the applied magnetic field H in the same range of temperatures. As shown in Fig. 10, as soon as $T<T_c$, a linear part emerges at low magnetic field values. It corresponds to the straight line of demagnetizing field. In the particular case of a ferromagneticlike transition where the magnetic susceptibility goes to infinity at the transition, this slope of this line is simply $1/N$, where N is the coefficient of demagnetizing field. Its origin should be purely geometric. Fitting this line provides an estimate of $1/N\approx 2.5$ and $N\approx 0.4$. This value is roughly consistent with crystallites of random orientation with respect to the applied field (here, the crystallites have approximatively elliptical shapes with a ratio length/diameter of 5 in average). Note the line of demagnetizing field is observed here in a polycrystalline mixture. It shows that the elementary crystal has not a purely uniaxial magnetic symmetry and should be more isotropic,[23] at least at the temperature of the ordering transition. Since the crystallites are needlelike, a quasi-one-dimensional character could be expected. An originality of the structure is that the chains of Fe^{II} are not along the longest dimension of the crystallites but in the plane which is orthogonal to it. As described above, these chains are also along two different directions. It is then likely that the magnetocrystalline energy favors the orientation of magnetic moments along these iron chains, giving an isotropic character in the spins direction.

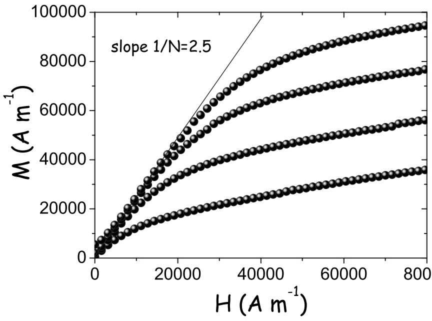

FIG. 10. Magnetization as a function of the increasing magnetic field, for temperatures $T=23$, 22, 21, and 20 K from bottom to top. The straight line is the line of demagnetizing field up to $H\sim 20\,000$ A/m$\sim$250 G at 20 K.

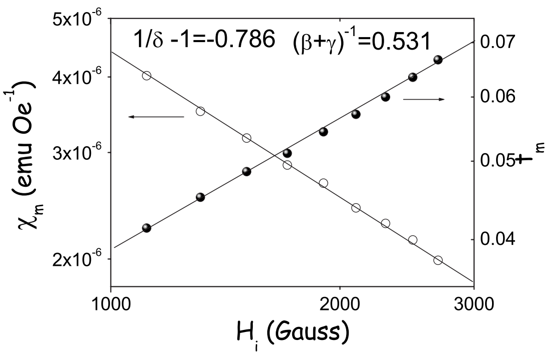

FIG. 11. Maximum of the in-phase susceptibility ($f=7$ Hz) as a function of the internal magnetic field H_i(corrected from the demagnetizing field) in log-log scale. Also shown is the reduced critical temperature as a function of H_i in log-log scale.

From this part, it can be concluded that the (field, temperature) range, where the slow dynamics of spin-glass-type appear, is directly linked to the demagnetizing effect close to the transition. It has to be associated with the presence and the growing of magnetic domains. In some aspects, it recall the Hopkinson effect of ferromagnetic which is observed in the low-field limit[24,25] but the frequency dependence that we observe indicate additional processes. The small frequency dependence is a characteristic of a slow dynamic, and implies here the presence of effective pinning centers which impede the growth and nucleation of magnetic domains. We have shown in the structural study that twin boundaries exist parallel to the iron chains, and can be responsible for local strains along which domain walls could corrugate. The size of the defects is few nanometers, which is a typical scale for domain walls. These extended defects are likely responsible for domain-wall pinning and for the associated slow dynamics. Interaction between twin boundaries and domain walls has been already reported in oxydes,[26] for example, domain walls were observed to be constraint by the twin direction using magneto-optical imaging.[27]

We have proposed potential defects which are important for impeding the growth and nucleation of magnetic domains in the magnetization process but they do not contribute to a large coercitive field. Indeed, our sample is a soft magnet with a coercitive field $H_c\approx 20$ G at $T=2$ K. We think that, as in amorphous material, the local disorder causes fluctuations of the anisotropy from one magnetic site to the other and the effective pinning potential for domains wall which are already formed is low. A consequence can be the existence of 3D rather than low-dimensional magnetic interactions at the sample scale, what can be studied with the analysis of critical exponents close to the ordering temperature.

C. Extraction of critical exponents and Bloch law

We have shown that the low-field regime $H<H^{*}$ is dominated by demagnetizing and pinning processes. Then, the genuine transition should be studied for $H>H^{*}$ when the variation in the apparent temperature of transition shows signs of a critical behavior (a decrease/broadening in the peak which moves to highest temperatures when the magnetic field is increased). This has been already emphasized by different authors, who have noted that the scaling laws of

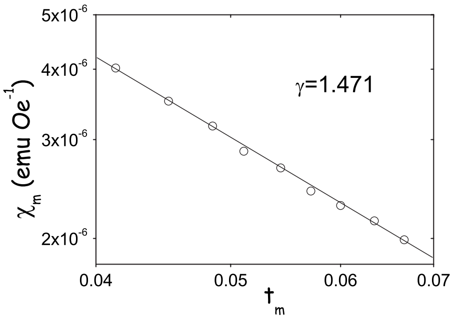

FIG. 12. Maximum of the in-phase susceptibility ($f=7$ Hz) as a function of the reduced temperature in log-log scale.

critical transition should be studied outside the range where technical processes dominate. Following Ref. 28, the position and value of the maximum of the ac susceptibility χ can be related to critical exponents as deduced from standard scaling theory. Using the reduced variables $t_m=T_m/T_c-1$ (T_m is the location of the susceptibility maximum) and $h=H_i/T_c$, where H_i is the internal field corrected from demagnetizing effect ($H_i=H-NM$), the following power-law dependences should be fulfilled:

$$\chi(H_i,t_m) \propto H_i^{(1/\delta)-1}, \tag{1}$$

$$t_m \propto H_i^{1/(\gamma+\beta)}, \tag{2}$$

$$\chi_m \propto t_m^{-\gamma}. \tag{3}$$

As shown in Figs. 11 and 12, the following values of critical exponents are found: $\delta=4.67\pm0.07$, $\gamma=1.47\pm0.03$, and $\beta=0.41\pm0.06$. These values are very close to those expected for a 3D Heisenberg isotropic magnet ($\delta=4.80$, $\gamma=1.39\pm0.09$, and $\beta=0.36$),[29] taken into account the experimental precision. This analysis confirms that interactions are long range and essentially 3D, and that random disorder of the structure does not impede significantly the long-range magnetic ordering.

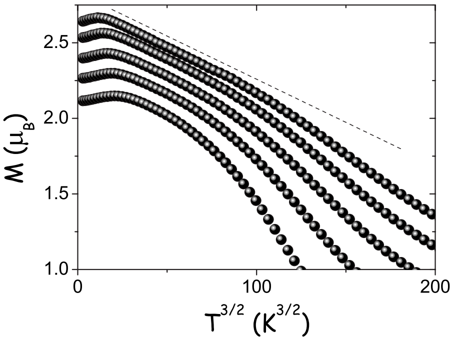

FIG. 13. Field-cooled magnetization as a function of $T^{3/2}$, for fields $H=1$, 2,3, 4, and 5 T from bottom to top. The dotted line corresponds to the temperature variation in the Bloch law which becomes apparent with the increase in the applied field. Note the decrease in the measured magnetization at low temperature, compared to the dotted line. The magnetization is per formula unit.

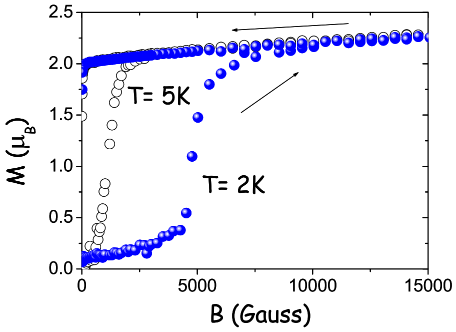

FIG. 14. (Color online) First magnetization curve as a function of the increasing and then decreasing magnetic field, for temperatures $T=5$ and 2 K, showing an irreversible metamagnetic transition. The magnetization is per formula unit.

In conventional ferromagnets (above technical saturation), but also when collinear ferrimagnetic structure is achieved at high enough magnetic field, the saturation magnetization M_s generally follows the Bloch law derived with spin waves theory. To first order, the increased spin waves excitation at higher temperature leads to $M_s \propto T^{3/2}$.[30] This is observed down to $T\leq 8$ K, where the moment decreases below its expected value (Fig. 13).

D. Reduction in the magnetic moment at low temperature

This low-temperature moment reduction suggests a breakdown of spin collinearity. The drop from the expected value of the magnetization at low temperature gives a relative reduction $r=0.94-0.97$, and would yield an averaged canting angle θ_c of $\theta_c=\arccos(r)\approx 14°-20°$.[31] Looking at the hysteresis loop at low temperature (Fig. 14), another effect is observed simultaneously: the virgin magnetization curve for $T<8$ K changes notably. The shape of this curve recalls a pinning type magnet but it lies outside the hysteresis loop boundary before saturation what is clearly unusual for a conventional magnet. We propose that the virgin magnetization reflects an irreversible metamagnetic transition, implying that the anisotropy is reinforced at low temperature. In such a case, the curve represents the irreversible rotation of one sublattice of magnetization with antiferromagnetic ground state at a critical field H_c (here $H_c\approx 0.45$ T at $T=2$ K). Goodenough-Kanamori exchange rules indicate an antiferromagnetic superexchange pathways in the chains containing the Fe$^{\mathrm{II}}$ ions. Metamagneticlike behavior implies also competing interactions and then ferromagnetic interactions (between next-nearest neighbor), which is consistent with the ferrimagnetism of the compound. We observe a remarkable increase in H_c between $T=5$ K and $T=2$ K (Fig. 14), in the temperature range where the canting occurs. It could arise from the reinforcement of the single-ion magnetic anisotropy of Fe$^{\mathrm{II}}$ ions as the temperature decreases. Another possibility is an antisymmetric Dzyaloshinsky-Moriya interaction which results from the anisotropic superexchange interaction,[32] and is allowed here because two neighboring Fe$^{\mathrm{II}}$ ions are not related by a center of inversion.

V. CONCLUSION

We have measured and discussed the magnetic properties of an original mixed-valency iron phosphate, focusing on the role of the complex structural disorder. Its random distribution at a nanoscale is responsible for the slow dynamics of magnetic domain walls as evidenced in the frequency dependence of the dynamical susceptibility but does not perturb significantly the long-range ferrimagnetic ordering, which is found of 3D Heisenberg type. At low temperature, the breakdown of the Bloch law indicates a spin canting. This implies a reinforced anisotropy at low temperature, which is likely responsible for the irreversible metamagnetic transition which appears in the same temperature range. This study shows how the role of disorder can be important, but can have also contrasted consequences, for magnetic properties.

---

[1] A. K. Padhi, K. S. Nanjundaswany, C. Masquelier, and J. B. Goodenough, J. Electrochem. Soc. **144**, 2581 (1997).

[2] F. Chen, M. H. Do, W. Zheng, D.-G. Cheng, and X. Zhan, Catal. Commun. **9**, 2481 (2008).

[3] N. N. Tušar, A. Ristić, A. Meden, and V. Kaučič, Microporous Mesoporous Mater. **37**, 303 (2000).

[4] S. Boudin, A. Guesdon, A. Leclaire, and M.-M. Borel, J. Inorg. Mater. **2**, 561 (2000).

[5] R. Nath, A. A. Tsirlin, E. E. Kaul, M. Baenitz, N. Büttgen, C. Geibel, and H. Rosner, Phys. Rev. B **78**, 024418 (2008).

[6] A. A. Tsirlin, R. Nath, C. Geibel, and H. Rosner, Phys. Rev. B **77**, 104436 (2008).

[7] A. A. Belik, M. Azuma, A. Matsuo, T. Kaji, S. Okubo, H. Ohta, K. Kindo, and M. Takano, Phys. Rev. B **73**, 024429 (2006).

[8] S. S. Salunke, M. A. H. Ahsan, R. Nath, A. V. Mahajan, and I. Dasgupta, Phys. Rev. B **76**, 085104 (2007).

[9] S. Neeraj, M. L. noy, and A. K. Cheetham, Solid State Sci. **4**, 397 (2002).

[10] C. Parada, J. Perles, R. Saez-Puche, C. Ruiz-Valero, and N. Snejko, Chem. Mater. **15**, 3347 (2003).

[11] A. Modaressi, A. Courtois, R. Gérardin, B. Malaman, and C. Gleitzer, J. Solid State Chem. **47**, 245 (1983).

[12] L. K. Elbouaanani, B. Malaman, R. Gérardin, and M. Ijjaali, J. Solid State Chem. **163**, 412 (2002).

[13] A. A. Belik, M. Azuma, M. Takano, and B. I. Lazoryak, Chem. Mater. **16**, 4311 (2004).

[14] A. A. Belik, Q. Huang, E. Takayama-Muromachi, and J. W. Lynn, J. Solid State Chem. **181**, 2292 (2008).

[15] M. Ijjaali, B. Malaman, C. Gleitzer, J. K. Warner, J. A. Hriljac and A. K. Cheetham, J. Solid State Chem. **86**, 195 (1990).

[16] O. Pérez, L. Adam, A. Guesdon, M. Daturi, and B. Raveau, Acta Crystallogr., Sect. B: Struct. Sci. **63**, 521 (2007).

[17] S. Boudin and K. W. Lii, Inorg. Chem. **37**, 799 (1998).

[18] J. A. Mydosh, *Spin Glasses* (Taylor & Francis, London, 1995).

[19] M. Giot, A. Pautrat, G. Andre, D. Saurel, M. Hervieu, and J. Rodriguez-Carvajal, Phys. Rev. B **77**, 134445 (2008).

[20] Eric Vincent in Ageing and the Glass Transition, Lecture Notes in Physics **716**, 7 (2007).

[21] The (H,T_m) points for $H < H^*$ vary as $(T-T_c)^{3/2}$, where T_c is the temperature of the zero-field susceptibility maximum. This dependence is similar of the Almeida-Thouless line of spin glasses (Ref. 22) but as other spinglasses properties are not verified, it is only incidental.

[22] J. R. L. de Almeida and D. J. Thouless, J. Phys. A **11**, 983 (1978).

[23] M. Rossignol and M. Schlenker, in *Magnetism: Fundamentals*, edited by E. du Trémolet de Lacheisserie, D. Gignoux, and M. Schlenker (EDP sciences, Grenoble, 2000).

[24] J. Hopkinson, Philos. Trans. R. Soc. London, Ser. A **180**, 443 (1889).

[25] G. Williams, J. Alloys Compd. **326**, 36 (2001).

[26] G. Popov, S. V. Kalinin, T. Alvarez, T. J. Emge, M. Greenblatt, and D. A. Bonnell, Phys. Rev. B **65**, 064426 (2002).

[27] G. Jung, V. Markovich, C. J. van der Beek, D. Mogilyansky, and Ya. M. Mukovskii, Phys. Rev. B **72**, 134412 (2005).

[28] W. Jiang, X. Z. Zhou, G. Williams, Y. Mukovskii, and K. Glazyrin, Phys. Rev. B **78**, 144409 (2008).

[29] J. C. Le Guillou and J. Zinn-Justin, Phys. Rev. B **21**, 3976 (1980).

[30] For example, N. W. Ashcroft and N. D. Mermin, *Solid State Physics* (Saunders, Philadelphia, 1976).

[31] T. Brown, W. Li, H. P. Kunkel, X. Z. Zhou, G. Williams, Y. Mukovskii, and A. Arsenov, J. Phys.: Condens. Matter **17**, 5997 (2005).

[32] I. Dzyaloshinsky, J. Phys. Chem. Solids **4**, 241 (1958); T. Moriya, Phys. Rev. **120**, 91 (1960).